

# 1 Subgrid corrections for the linear inertial equations of a compound 2 flood model – a case study using SFINCS 2.1.1 Dollerup release

3 Maarten van Ormondt<sup>1</sup>, Tim Leijne<sup>2,3</sup>, Roel de Goede<sup>2</sup>, Kees Nederhoff<sup>1</sup>, Ap van Dongeren<sup>2,4</sup>

4 <sup>1</sup> Deltares USA, 8601 Georgia Ave, Silver Spring, MD 20910, USA

5 <sup>2</sup> Marine and Coastal Management, Deltares, Boussinesqweg 1, Delft, 2629 HV, The Netherlands

6 <sup>3</sup> Institute for Environmental Studies (IVM), Vrije Universiteit Amsterdam, De Boelelaan 1111, 1081 HV Amsterdam, The  
7 Netherlands.

8 <sup>4</sup> Coastal and Urban Risk & Resilience Dept, IHE Delft, Westvest 7, 2611 AX Delft, The Netherlands

9 *Correspondence to:* Kees Nederhoff ([kees.nederhoff@deltares-usa.us](mailto:kees.nederhoff@deltares-usa.us))

10 **Keywords.** Hydrodynamic modeling, subgrid, Linear Inertial Equations, compound flooding, SFINCS

11

12 **Abstract.** Accurate flood risk assessments and early warning systems are needed to protect and prepare people in coastal areas  
13 from storms. In order to provide this information efficiently and on time, computational costs in flood models need to be kept  
14 as low as possible. One way to achieve this goal is to apply subgrid corrections to relatively coarse computational grids.  
15 Previously, these have been used in full-physics circulation models. In this paper, for the first time, we developed subgrid  
16 corrections for the Linear Inertial Equations (LIE) that account for bed level and friction variations. They were implemented  
17 in the SFINCS model version 2.1.1 Dollerup Release. Pre-processed lookup tables that correlate water levels with  
18 hydrodynamic quantities make more precise simulations with lower computational costs possible. These subgrid corrections  
19 have undergone validation through several conceptual and real-world application scenarios, including rainfall-induced  
20 flooding during a hurricane and tidal propagation in an estuary. We demonstrate that the subgrid corrections for Linear Inertial  
21 Equations significantly improve model accuracy while utilizing the same resolution without subgrid corrections. In terms of  
22 computational efficiency, subgrid corrections increase computational costs by 38-128%. However, they yield a 35-50 times  
23 speedup since coarser model resolutions with subgrid corrections can provide the same accuracy as finer resolutions without  
24 subgrid corrections. Limitations are discussed, for example, when grids do not adequately resolve river meanders, fluxes can  
25 be overestimated. Our findings show that subgrid corrections are a useful asset for hydrodynamic modelers striving to achieve  
26 a balance between accuracy and efficiency.

## 27 1 Introduction

28 With hundreds of millions of people living in areas with an elevation of less than 10 meters above sea level (McGranahan et  
29 al, 2007), coastal zone flooding has large consequences for casualties and damage to real estate and infrastructure. To protect  
30 and mitigate flood damages and loss of life, a priori risk assessments may inform decision makers in what locations and under  
31 what circumstances flooding occurs, and what interventions to take. Both the risk assessments and early warning systems  
32 should provide as accurate as possible information so as not to give false warnings or needlessly over or underestimate the  
33 extent and cost of interventions.

34  
35 For flood warnings, this means that simple bathtub approaches, where a peak water level is imposed on an area's topography,  
36 do not suffice. They may overestimate the flood intensity because the surge hydrograph is not taken into account (Vousdoukas  
37 et al., 2016) or underestimate it due to lacking physics (e.g. wave effects, Didier et al., 2020) or lacking inputs such as roughness  
38 effects which would impede flow (Ramirez et al., 2016). Therefore, for a more accurate flood estimate, the dynamic aspects  
39 of floods such as the duration of an event, and the path that flood waters take should be considered. Furthermore, the compound  
40 nature of coastal area floods, which may be caused by a combination of marine surges, wave overtopping, coastal river  
41 discharges, and local rainfall needs to be taken into account. These dynamics and processes may be resolved using process-  
42 based numerical models which are based on the conservation of mass and momentum. While classical full-physics models  
43 (ADCIRC; Luetlich et al., 1992, Delft3D-FLOW; Lesser et al., 2004, MIKE; Warren and Bach, 1992 or SOBEK; Stelling et  
44 al., 1998) offer highly detailed simulations, they often require substantial computational resources, particularly for high-  
45 resolution simulations over large areas or when exploring uncertainties in flooding through ensemble modeling. Although  
46 these models can be applied to large-scale systems with adequate computing power, their high computational demands may  
47 constrain their practical use in time-sensitive or resource-limited scenarios.

48  
49 To that end, reduced-complexity models have been developed and applied in riverine settings and coastal applications.  
50 Examples include, among others, the LISFLOOD-FP model by Bates et al. (2010) and the SFINCS (Super-Fast INundation of  
51 CoastS) model by Leijnse et al. (2021). These models focus on solving reduced forms of the momentum equations using a  
52 simplified numerical scheme, allowing them to run significantly faster than traditional full-physics models. Still, the number  
53 of simulations that can be run is limited, as the numerical scheme is explicit and therefore strongly influenced by the spatial  
54 grid size (and associated time step).

55  
56 One way to further increase the computational speed is to apply a subgrid approach which makes use of the assumption that  
57 water level gradients are typically much smaller than topographic gradients. Defina (2000) presented shallow water equations  
58 with mass conservation corrections to account for wetting and drying areas, and corrections to the momentum equations to  
59 account for varying velocities. Casulli (2009a) introduced a dual-grid approach with a higher resolution grid for the bathymetry

60 and a lower resolution grid for the hydrodynamics where the depth and cross-sectional area were computed using the higher-  
61 resolution grid and stored in lookup tables which were used to evaluate the water levels on the lower resolution grid. Volp et  
62 al. (2013) extended Casulli's approach to finite volumes and incorporated subgrid corrections to compute advection and bottom  
63 friction under the assumptions of locally uniform flow direction and friction slope. Sehili et al. (2014) showed that subgrid  
64 corrections could save an order of magnitude of computational cost without major accuracy loss in estuarine modeling. For  
65 coastal storm surge applications, Kennedy et al. (2019) developed a refined set of equations incorporating extra terms derived  
66 from an upscaling technique. These additional terms, emerging from the averaging of shallow water equations, account for the  
67 integral properties of fine-scale bathymetry, topography, and flow dynamics. This process is similar to how Boussinesq  
68 approximations are used for turbulence closure in Navier-Stokes models and involves using coarse-scale variables, such as  
69 averaged fluid velocity, to represent these fine-scale integrals. They showed the improved performance of their model for the  
70 case of tidal flooding in a small bay. Woodruff et al. (2021) extended this analysis to a case of storm surge with realistic  
71 atmospheric forcing and reported a speedup of ADCIRC with a factor of 10-50. Similarly, Begmohammadi et al. (2023)  
72 adapted the numerical implementation of the real-time forecasting model SLOSH (Jelesnianski and Chester, 1992) to improve  
73 inundation performance in a coastal region with narrow channels. Woodruff et al. (2023) scaled up these approaches to the  
74 entire South Atlantic Bight and showed improved performance of a subgrid model to a conventional high-resolution model for  
75 Hurricane Matthew (2016).

76

77 More recently, subgrid models such as CoaSToRM (Begmohammadi et al., 2024) and HEC-RAS (Brunner, 2016) have further  
78 advanced the field. CoaSToRM is a standalone solver for compound flooding in coastal regions, utilizing subgrid topography  
79 to improve inundation accuracy in overland and coastal flood modeling. HEC-RAS nowadays also allows for the integration  
80 of subgrid corrections, utilizing detailed hydraulic property tables to improve performance in both riverine and coastal flood  
81 scenarios.

82

83 While these advances have led to great improvements in estuarine and storm surge modeling, the assumption of hydraulic  
84 connectivity of subgrid cells remains a challenge. To that end, Casulli (2009b) and Begmohammadi et al. (2021) removed the  
85 artifact of flows occurring through catchment boundaries that are not resolved by subgrid corrections by restricting flow to a  
86 predetermined path. Rong et al. (2023) introduced a new diffusive scheme in the existing subgrid corrections approach to better  
87 model flood routing in rivers and adjacent flood plains. Yu and Lane (2011) applied subgrid corrections to resolve the  
88 roughness effects of small-scale structural elements in river floodplain cases, based on the method by Yu and Lane (2006) and  
89 applied a storage correction to the coarser scale flow grid based on the higher-resolution topographic information accounting  
90 for cell blockage and conveyance effects.

91

92 However, none of these efforts combined a reduced-complexity model with subgrid corrections that account for bed level and  
 93 friction variations for efficient compound flood modeling. In this paper, we explore subgrid corrections for the Linear Inertial  
 94 Equations (Bates et al., 2010) that are used in the SFINCS model (Leijnse et al., 2021). All model results were obtained with  
 95 the SFINCS ‘Dollerup release from November 2023 which is available as open-source code on GitHub and via  
 96 <https://www.deltares.nl/en/software-and-data/products/sfincs> (van Ormondt et al., 2024). Computational speeds reported in  
 97 this paper are determined by running the simulations on an Intel core I9 10980XE CPU.

98

99 The paper is organized as follows: we start with the governing equation in SFINCS, and a description of the new subgrid  
 100 corrections (Section 2). We then demonstrate the accuracy of the subgrid corrections for some conceptual cases (Section 3).  
 101 In Section 4, the subgrid corrections are verified against the default SFINCS results and observed data for two real-world  
 102 cases: tidal propagation at the St. Johns River (Florida, USA) and the flooding during Hurricane Harvey (Houston, USA). The  
 103 findings are discussed in Section 5 and our conclusions are presented in Section 6.

## 104 2 Model description

### 105 2.1 SFINCS governing equations

106 The SFINCS model solves the shallow-water equations on a regular, staggered Arakawa-C grid. Its governing equations are  
 107 based on the Linear Inertial Equations (LIEs; Bates et al., 2010). In particular, the volumetric flow rate per unit width at the  
 108 interface between adjacent cells in the  $x$  direction for the current time step is computed with Equation 1:

$$109 \quad q_u^{t+\Delta t} = \frac{q_u^t - g\Delta t h_u \frac{\Delta z}{\Delta x} + F\Delta t}{1 + g\Delta t n^2 |q_u^t| / h_u^{7/3}} \quad (1)$$

110 where  $q_u^t$  is the flow rate at the previous time step,  $h_u$  and  $\Delta z/\Delta x$  are the water depth and water level gradient at the cell interface  
 111  $u$ ,  $g$  is the acceleration constant,  $n$  is the Manning’s  $n$  roughness and  $\Delta t$  is the time step. The water depth  $h_u$  at the cell interface  
 112 is computed in SFINCS as the difference between the maximum water level in the two adjacent cells and the maximum bed  
 113 level in these cells. For the sake of brevity, additional forcing terms, such as wind drag, barometric pressure gradients, and the  
 114 advection term, are represented in the combined term  $F$ .

115

116 The mass continuity equation reads:

$$117 \quad z_s^{t+\Delta t} = z_s^t + \Delta t \left( \frac{q_{u\ m-1,n}^t - q_{u\ m,n}^t}{\Delta x} + \frac{q_{v\ m,n-1}^t - q_{v\ m,n}^t}{\Delta y} + \frac{S_{m,n}}{\Delta x \Delta y} \right) \quad (2)$$

118 where  $z_s$  is the water level in a grid cell (with index  $m$  in  $x$ -direction,  $n$  in  $y$ -direction), and  $S_{m,n}$  is an (optional) source term in  
 119  $\text{m}^3/\text{s}$  which can be positive and negative (e.g. to represent precipitation, infiltration or a user-defined point source). SFINCS

120 allows for the specification of either constant in-time infiltration rates or empirical rainfall-runoff models such as the Curve  
121 Number method, the Green-Ampt method, and the Horton infiltration method. In the remainder of this document, formulations  
122 will often be presented in the  $x$  direction, with the  $y$  direction treated analogously (with cell interface  $v$ ).

123

124 SFINCS uses a first-order explicit backward in time with a first-order central difference approximation of the spatial derivatives  
125 (BTCS-scheme).

## 126 2.2 Subgrid corrections in the momentum equation

127 The goal of the subgrid corrections is to compute flooding in a computationally efficient way using larger grids while retaining  
128 information of the higher-resolution elevation and roughness data. This is achieved by adjusting the conveyance depth  $h_u$  and  
129 Manning’s roughness  $n$  in Equation 1 based on the local water level  $z_u$  and the subgrid topography and roughness so that the  
130 unit discharge  $q_u$  through a cell interface equals the average of the unit discharge of the subgrid pixels within the considered  
131 velocity point. An important assumption here is that the water level within the velocity point is constant, and therefore equal  
132 for all subgrid pixels. If the subgrid topography is known, and we assume that the water level  $z_u$  is constant for all subgrid  
133 pixels in the velocity point, then representative values for  $h_u$  and  $n$  (as well as the wet fraction  $\varphi$ ) can be computed as a function  
134 of  $z_u$  and stored in lookup tables for each velocity point. During a simulation, these lookup tables are queried at each time step  
135 to provide representative values for  $h_u$ ,  $n$ , and  $\varphi$ . This section explains the theory behind the subgrid corrections for the LIEs.  
136 The following sections describe the practical generation of the subgrid tables, and how these are queried during a SFINCS  
137 simulation.

138

139 Following the notation of Kennedy et al. (2019), for a quantity  $Q$ , hydrodynamic variables coarsened to the grid scale are  
140 defined as:

$$141 \quad \langle Q \rangle_G = \frac{1}{A} \iint_{A_W} Q dA \quad (3)$$

142 where  $A_W$  is the wet portion of the grid cell area  $A$ . This will be called the “grid average” and is denoted with subscript “G”.

143

144 On the other hand, the “wet average” of  $Q$ , denoted with subscript “W” is:

$$145 \quad \langle Q \rangle_W = \frac{1}{A_W} \iint_{A_W} Q dA \quad (4)$$

146

147 with the wet average area is defined as:

$$148 \quad A_W = \varphi A \quad (5)$$

149 where  $\varphi$  is the wet fraction of the cell area, then for hydrodynamic quantity  $Q$ :

150  $\langle Q \rangle_G = \varphi \langle Q \rangle_W$  (6)

151

152 Rewriting Equation 1 using wet average quantities yields the LIEs in their subgrid form :

153 
$$\langle q_u \rangle_W^{t+\Delta t} = \frac{\langle q_u \rangle_W^t - g \Delta t \langle H_u \rangle_W \frac{\Delta z}{\Delta x} + F \Delta t}{1 + g \Delta t n_{u,W}^2 |\langle q_u \rangle_W^t| / \langle H_u \rangle_W^{7/3}}$$
 (7)

154 where  $\langle q_u \rangle_W$  and  $\langle H_u \rangle_W$  are the wet average unit discharge and water depth, respectively..  $n_{u,W}$  is the Manning's n coefficient  
 155 adjusted for subgrid variations.

156

157 The expression for  $n_{u,W}$  can be derived by considering Manning's equation for open channel flow:

158 
$$\langle q_u \rangle_W = \sqrt{i} \frac{\langle H_u \rangle_W^{5/3}}{n_{u,W}}$$
 (8)

159 where  $i$  is the water level slope  $\frac{\Delta z_s}{\Delta x}$ . In case of a stationary current and in the absence of external forcing, the subgrid form of  
 160 the LIEs reverts to Equation 8. Consider now a velocity point with  $N$  subgrid pixels, each with its own bed level  $z_{b,k}$  and  
 161 roughness  $n_k$  (see Figure 1). For a water level  $z_u$ , the water depth in each pixel is  $h_k = \max(z_u - z_{b,k}, 0)$ . The wet average unit  
 162 discharge of the subgrid pixels within the velocity point is:

163 
$$\langle q_u \rangle_W = \frac{1}{\varphi_u N} \sqrt{i} \sum_{k=1}^N \frac{h_k^{5/3}}{n_k}$$
 (9)

164 where  $\varphi_u N$  is the number of wet pixels. Equation 9 can also be written as:

165 
$$\langle q_u \rangle_W = \sqrt{i} \left\langle \frac{H_u^{5/3}}{n} \right\rangle_W$$
 (10)

166

167 Substituting Equation 10 into Equation 8 yields the expression for  $n_{u,W}$  (Equation 11):

168 
$$n_{u,W} = \frac{\langle H_u \rangle_W^{5/3}}{\left\langle \frac{H_u}{n} \right\rangle_W}$$
 (11)

169

170 The subgrid form of the LIEs (Equations 7 and 11) can alternatively be expressed with “grid average” quantities. The SFINCS  
 171 model uses these to solve the momentum balance, rather than the “wet average” quantities described above. Although  
 172 somewhat less intuitive, using grid average quantities has a few practical advantages that will be discussed in the next section.  
 173 To write the subgrid form of the LIEs using grid average quantities we simply substitute  $\langle q_u \rangle_W$  with  $\langle q_u \rangle_G / \varphi_u$  and  $\langle H_u \rangle_W$   
 174 with  $\langle H_u \rangle_G / \varphi_u$  in Equation 7:

175 
$$\langle q_u \rangle_G^{t+\Delta t} = \frac{\langle q_u \rangle_G^t - g \Delta t \langle H_u \rangle_G \frac{\Delta z}{\Delta x} + \varphi_u F \Delta t}{1 + g \Delta t n_u^2 |\langle q_u \rangle_G^t| / \langle H_u \rangle_G^{7/3}} \quad (12)$$

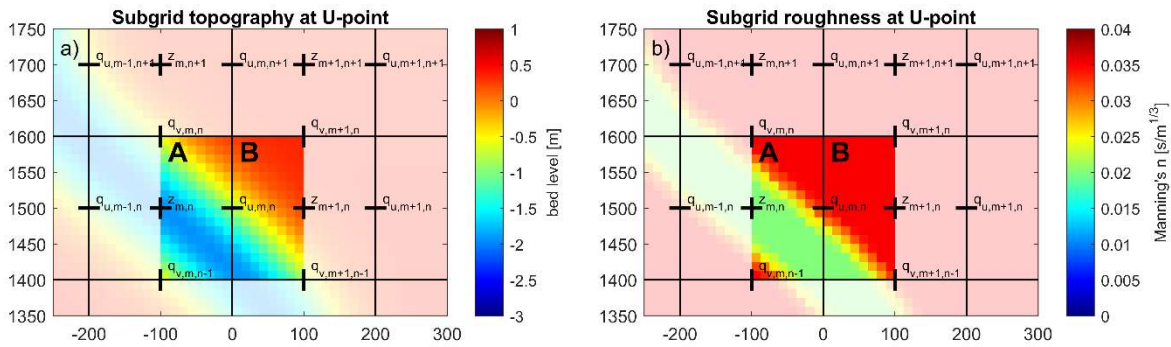
176 where  $n_u$  is  $\varphi_u^{2/3} n_{u,W}$ .

177

178 Using the same logic as for Equation 11,  $n_u$  (hereafter called the representative roughness) can also be written as:

179 
$$n_u = \frac{\langle H_u \rangle_G^{5/3}}{\langle \frac{H_u}{n} \rangle_G} \quad (13)$$

180 For a known subgrid topography, and assuming a constant water level  $z_u$  for all subgrid pixels in the velocity point,  $\langle H_u \rangle_G$ ,  $n_u$ ,  
 181 and  $\varphi_u$  can be stored in lookup tables as a function of  $z_u$ . The generation of such tables is a pre-processing step that occurs only  
 182 once when the model is set up, and is not repeated in the computational loop. First, a subgrid is generated that has the same  
 183 orientation as the coarser hydrodynamic grid and a higher resolution. The level of refinement of the subgrid is an even integer  
 184 and is typically chosen such that the subgrid resolution roughly equals that of the digital elevation model (DEM). Next, the  
 185 subgrid model bathymetry is generated by interpolating a high-resolution DEM onto the subgrid. The roughness values are  
 186 determined at the subgrid-scale as well, for example by converting data from land use maps to Manning's  $n$  values and  
 187 interpolating these onto the subgrid. An example of topography and roughness on the subgrid at a velocity point is provided  
 188 in Figure 1. Specifically, the high-resolution subgrid topography and roughness values around a single velocity point  
 189 demonstrate that information from both sides (A and B) of the water level grid cell is included in calculating the flux over the  
 190 cell face  $q_{u,m,n}$  between  $z_{m,n}$  and  $z_{m+1,n}$ .



191

192 **Figure 1. High-resolution values of elevation  $z$  (panel a) and roughness  $n$  (panel b) at a U velocity point with a subgrid pixel resolution**  
 193 **of  $N=16 \times 16$  per computational cell. Colors for elevation and roughness indicate subgrid-scale values which are aggregated on the**  
 194 **computational black grid cells. Water level points are indicated by '+', while velocity points are marked with '-' and 'q'.**

195

196 Values for the subgrid momentum corrections in SFINCS are only computed at discrete equidistant vertical levels, ranging  
 197 between  $z_{min}$  and  $z_{max}$ . For each velocity point, we distinguish between two sides A and B of a computational cell (see Figure  
 198 1). The minimum ( $z_{b,A,min}$  and  $z_{b,B,min}$ ) and maximum ( $z_{b,A,max}$  and  $z_{b,B,max}$ ) pixel elevations at both sides are determined. The  
 199 combined minimum and maximum elevations  $z_{min}$  and  $z_{max}$  are defined as:

$$200 \quad z_{min} = \max(z_{b,A,min}, z_{b,B,min}) \quad (14)$$

$$201 \quad z_{max} = \max(z_{b,A,max}, z_{b,B,max}) \quad (15)$$

202

203 Values of  $\langle H_u \rangle_G$ ,  $\langle \frac{H_u^{5/3}}{n} \rangle_G$ , and  $\varphi_u$  are now computed for both sides A, B separately, and for the combined total velocity point (A  
 204 + B) at all vertical levels between  $z_{min}$  and  $z_{max}$ . If M is the number of vertical levels, the vertical distance between each level  
 205 is defined as  $\Delta z = (z_{max} - z_{min}) / (M - 1)$ , and the elevation of each discrete level is  $z_m = z_{min} + (m - 1) \Delta z$  (in which m goes  
 206 from 1 to M).

207

208

209 Values for  $\langle H_u \rangle_{G,m}$  and  $n_{u,m}$  at each level between  $z_{min}$  and  $z_{max}$  are obtained by taking a weighted average of the values at  
 210 sides A, B and the combined A + B. The aim of the weighting procedure is to ensure that the grid-averaged depth  $\langle H_u \rangle_G$  (and  
 211 therefore the water flux) at dry velocity points ( $z_u = z_{min}$ ) is 0, whereas for completely wet points ( $z_u = z_{max}$ ),  $\langle H_u \rangle_{G,M}$  and  $n_{u,M}$   
 212 are determined with all subgrid pixels (i.e. using A + B). This is achieved by letting the weight factor vary over the vertical,  
 213 using the wet fractions  $\varphi_{u,A}$  and  $\varphi_{u,B}$  (Equation 16):

214

$$215 \quad w_m = \min(\varphi_{u,m,A}, \varphi_{u,m,B}) / \max(\varphi_{u,m,A}, \varphi_{u,m,B}) \quad (16)$$

216

217 At the lowest level ( $z_m = z_{min}$ ),  $w_m$  is 0 by definition (since either  $\varphi_{u,m,A}$  or  $\varphi_{u,m,B}$  is 0 here), whereas at the highest level ( $z_m$   
 218 =  $z_{max}$ )  $w_m$  is always 1. The values for  $\langle H_u \rangle_{G,m}$  and  $n_{u,m}$  that are stored in the subgrid tables are determined with Equations  
 219 17 to 19:

220

$$221 \quad \langle H_u \rangle_{G,m} = (1 - w_m) \min(\langle H_u \rangle_{G,m,A}, \langle H_u \rangle_{G,m,B}) + w_m \langle H_u \rangle_{G,m,A+B} \quad (17)$$

$$222 \quad \langle \frac{H_u^{5/3}}{n} \rangle_{G,m} = (1 - w_m) \min \left( \langle \frac{H_u^{5/3}}{n} \rangle_{G,m,A}, \langle \frac{H_u^{5/3}}{n} \rangle_{G,m,B} \right) + w_m \langle \frac{H_u^{5/3}}{n} \rangle_{G,m,A+B} \quad (18)$$



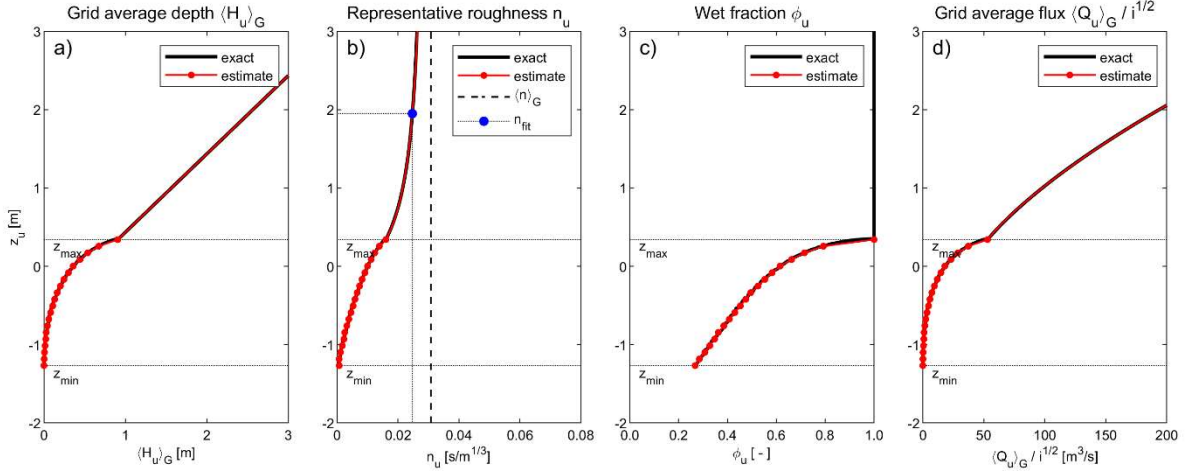
223

$$n_{u,m} = \frac{\langle H_u \rangle_{G,m}^{5/3}}{\langle \frac{H_u}{n} \rangle_{G,m}^{5/3}} \quad (19)$$

224

225 The subgrid tables and resulting flux (panel d) for the velocity point depicted in Figure 1, using  $M=20$  are illustrated in Figure

226 2. Red markers highlight the values at the discrete vertical levels.



227

228 **Figure 2. Computation of subgrid quantities  $\langle H_u \rangle_G$  (panel a),  $n_u$  (panel b) and  $\phi_u$  (panel c) as a function of water level  $z_u$  with 20**  
 229 **discrete vertical levels ( $M = 20$ ). The resulting flux divided by the square root of the water slope  $i$  is shown in panel d. The black line**  
 230 **shows the exact solution obtained by solving Equations 5, 10, 11 and 17. The red line shows the estimate used in the SFINCS model,**  
 231 **with (for  $z \leq z_{max}$ ) linear interpolation of lookup table values, and (for  $z > z_{max}$ ) linear increase for  $\langle H_u \rangle_G$  and fit for  $n_u$ .**

232 At each time step during a simulation, the model computes the water level  $z_u$  at each velocity point using the maximum of the  
 233 computed water levels in the two adjacent cells, i.e.  $z_u = \max(z_{s_{m,n}}, z_{s_{m+1,n}})$ . This value is then used to query the lookup  
 234 tables to find appropriate values of the quantities  $\langle H_u \rangle_G$ ,  $n_{u,m}$ , and  $\phi_{u,m}$ . For partially wet velocity points ( $z_{min} < z_{u,m} < z_{max}$ ),  
 235 a linear interpolation of the values in the tables is used. When the entire velocity point is wet ( $z_u \geq z_{max}$ ), the depth  $\langle H_u \rangle_G$   
 236 increases linearly with  $z_u$  (Figure 2a and Equation 20):

$$\langle H_u \rangle_G = \langle H_u \rangle_{G,M} + z_u - z_{max} \quad (20)$$

237

238  
 239 The determination of  $n_u$  for completely wet velocity points is more complicated, due to its non-linear relationship with  $z_u$  at  $z_u$   
 240  $> z_{max}$  (see Figure 2b). It would be possible to store values of  $n_u$  at many levels above  $z_{max}$  in the subgrid tables, but that could  
 241 result in very large file sizes and memory use. To avoid this, SFINCS uses the following estimation for  $n_u$  instead:

242

$$n_u = \langle n \rangle_G - \frac{\langle n \rangle_G - n_{u,M}}{\beta(z_u - z_{max}) + 1} \quad (21)$$

243 where  $\langle n \rangle_G$  is the average Manning's  $n$  of all subgrid pixels, and  $\beta$  is a fitting coefficient (with both these parameters also  
 244 stored in the subgrid tables). The fitting coefficient  $\beta$  is determined for each velocity point with Equation 22.

$$245 \quad \beta = \frac{\langle n \rangle_G - n_{u,M} - 1}{\langle n \rangle_G - n_{fit}} \frac{z_{fit} - z_{max}}{z_{fit} - z_{max}} \quad (22)$$

246  
 247 Here we have defined the level  $z_{fit}$  at  $z_{max} + (z_{max} - z_{min})$ . The value for  $n_{fit}$  at  $z_{fit}$  is determined like Equation 19:

$$248 \quad n_{fit} = \frac{(\langle H_u \rangle_{G,M} + z_{fit} - z_{max})^{5/3}}{\frac{1}{N} \sum_{k=1}^N \left( \frac{z_{fit} - \max(z_{b,k}, z_{min})}{n_k} \right)^{5/3}} \quad (23)$$

249 The estimated value for  $n_u$  above  $z_{max}$  using Equation 21 is shown in Figure 2b, with the blue marker indicating  $n_{fit}$ . In very  
 250 deep water ( $z_u \gg z_{max}$ ),  $n_u$  approaches  $\langle n \rangle_G$ , whereas for  $z_u = z_{max}$ ,  $n_u$  is equal to  $n_{u,M}$ .

251  
 252 The behavior of  $n_u$  in Figure 2b can seem non-intuitive. Whereas the grid average water depth  $\langle H_u \rangle_G$  has a real physical  
 253 meaning, the representative roughness  $n_u$  should not be interpreted as a physical quantity but rather as a quantity that is used  
 254 to control the flux through a velocity point, given a certain grid average water depth  $\langle H_u \rangle_G$  and water slope  $i$ . It is a function  
 255 not only of the physical subgrid roughness but also of the subgrid water depth.

256  
 257 The number ( $M$ ) of discrete vertical levels in the subgrid tables is defined by the user. We have found that around 20 levels  
 258 are typically sufficient to accurately describe the subgrid quantities  $\langle H_u \rangle_G$ ,  $n_u$  and  $\varphi_u$  as a function of water levels between  $z_{min}$   
 259 and  $z_{max}$  and is used throughout this paper. However, it is recommended to do a sensitivity analysis in order to find an optimal  
 260 number of vertical levels. This can be done by running multiple simulations with an increasing number of levels. As the number  
 261 of levels increases, the simulation results will converge. Ideally, the number of vertical levels should not significantly alter the  
 262 simulation results and still result in an acceptable file size of the subgrid table file.

263  
 264 As mentioned previously, SFINCS uses grid average, rather than wet average quantities. Theoretically, both options would  
 265 yield identical results. The reason to choose a grid average approach is that the wet average depth and adjusted roughness can  
 266 vary much more rapidly and irregularly with changing water levels than their grid average equivalents. As a result, many more  
 267 vertical levels in the subgrid tables would be required to accurately describe wet average quantities as a function of  $z$ .

### 268 **2.3 Subgrid corrections in the continuity equation**

269 The subgrid continuity equation is written in terms of grid average fluxes as:

270 
$$V_{m,n}^{t+\Delta t} = V_{m,n}^t + \Delta t \left( (\langle q_u \rangle_{G,m-1,n}^t - \langle q_u \rangle_{G,m,n}^t) \Delta y + (\langle q_v \rangle_{G,m,n-1}^t - \langle q_v \rangle_{G,m,n}^t) \Delta x + S_{m,n} \right) \quad (24)$$

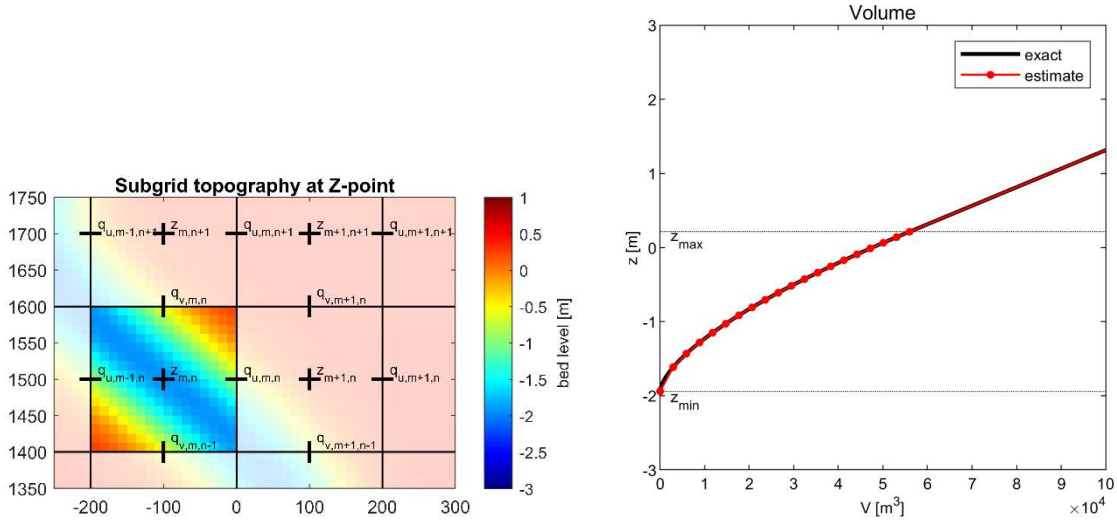
271 Contrary to Equation 2, Equation 24 computes the wet volume at the next time step, rather than the water level. The  
 272 corresponding water level  $z_s$  is obtained from the continuity subgrid tables.

273

274 To generate the subgrid tables first the minimum and maximum pixel elevations  $z_{min}$  and  $z_{max}$ , as well as the wet volume  $V_{max}$   
 275 (defined as the wet volume between  $z_{min}$  and  $z_{max}$ ) are determined for each hydrodynamic grid cell (e.g. Figure 3). Then the  
 276 wet volume as a function of the local water level is determined with Equation 25:

277 
$$V(z) = \frac{\Delta x \Delta y}{N} \sum_{k=1}^N \max(z - z_k, 0) \quad (25)$$

278 where  $N$  is the number of subgrid pixels in a grid cell. Finally, a number ( $M$ ) of discrete equidistant volumes are defined,  
 279 ranging between 0 and  $V_{max}$ , where each volume is  $V_m = (m - 1) V_{max} / (M - 1)$ . By iterating over each discrete volume  $V_m$ , we  
 280 can (using linear interpolation of Equation 24) determine the corresponding water levels  $z_s$ . An example is given in Figure 3  
 281 which shows the volumes of the highlighted cell.



282  
 283 **Figure 3. Panel A: values on the subgrid-scale of elevation  $z$  at a water level point ( $N=16 \times 16$ ). Panel B. Representation of water level**  
 284  **$z_s$  as a function of volume  $V$  with 20 discrete volumes ( $M = 20$ ). The black line shows the exact solution of Equation 24. The red line**  
 285 **shows the estimate of  $z_s$  used in the SFINCS model with, for  $z_s \leq z_{max}$ , linear interpolation of lookup table values, for  $z_s > z_{max}$  a**  
 286 **linear increase with  $V$ .**

287 During a simulation, the model computes at each time step the volume  $V$  in each cell and queries the lookup tables to find the  
 288 matching value for  $z_s$ . For partially wet cells ( $V < V_{max}$ ), a linear interpolation of the values in the tables is used. When the  
 289 entire cell is wet ( $V \geq V_{max}$ ), the water level  $z_s$  increases linearly with  $V$  and is computed as

$$z_s = z_{max} + \frac{V - V_{max}}{\Delta x \Delta y} \quad (26)$$

290

291 Note that for pre-processing purposes, it would have been more straightforward to describe the wet volume  $V$  at equidistant  
292 vertical levels  $z_m$  (similar to the approach for the momentum subgrid tables). However, during the simulation, the linear  
293 interpolation of subgrid data with equidistant volume levels is much more efficient.

## 294 **2.4 Pre and post-processing**

295 Pre-processing steps for SFINCS include creating a mask file describing (in)active cells, interpolating bathymetry and  
296 roughness values, and imposing boundary conditions. Tools to carry out these steps are available in both Delft Dashboard (Van  
297 Ormondt et al., 2020) and HydroMT-SFINCS (Eilander et al., 2024 or [https://deltares.github.io/hydromt\\_sfincs/latest/](https://deltares.github.io/hydromt_sfincs/latest/)), which  
298 both also have the capability to generate subgrid table files using high-resolution DEMs. In generating these subgrid tables,  
299 we largely follow common international standards such as NetCDF, ensuring compatibility and consistency with widely  
300 accepted practices in hydrodynamic modeling.

301

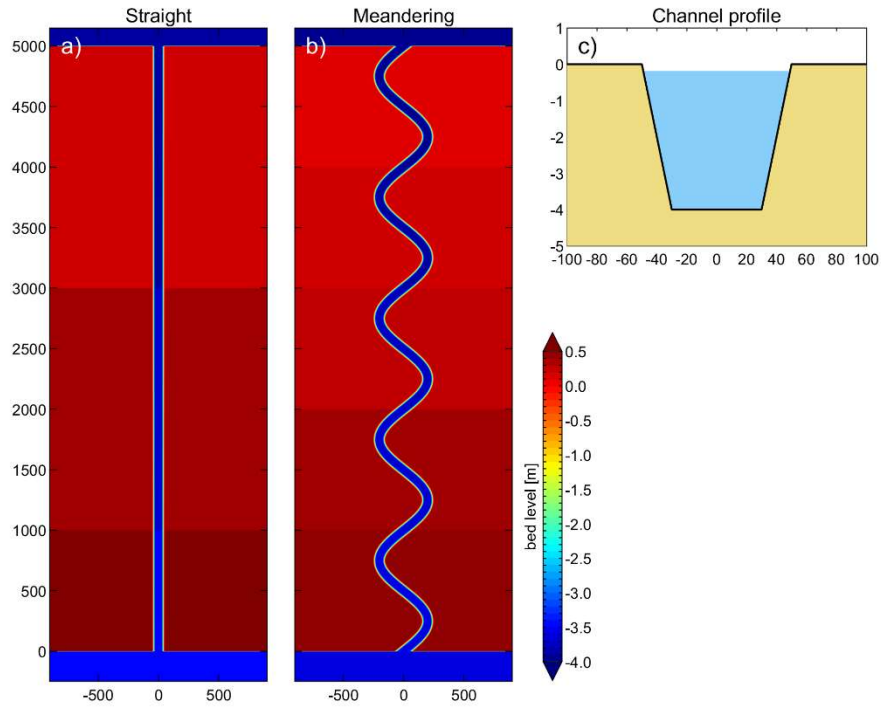
302 SFINCS stores the output of hydrodynamic quantities on the (coarse) computational grid. These results can be further  
303 downscaled to higher-resolution flood maps at the original DEM resolution (assuming again that the computed water level in  
304 a grid cell is representative of each subgrid pixel within that cell). Flood depths at the DEM scale are computed by subtracting  
305 the elevation of each DEM pixel from the water level in the cell. An example of the results is presented in Figure 10.

## 306 **3 Conceptual verification cases: straight and meandering channels**

307 The first conceptual test involves a 5 km long straight channel of 100 m wide with 1:5 side slopes (Figure 4a and c), for which  
308 a synthetic bathymetry was created. The slope of the channel is  $10^{-4}$  downhill in y-direction, and the flood plains on either side  
309 of the channel have an elevation of 0.3 m above the water level in the channel. The Manning's  $n$  roughness is set to  $0.02 \text{ s/m}^{1/3}$ .  
310 Water level boundary conditions at the upstream and downstream sides are set to +0.25 m and -0.25 m, respectively, resulting  
311 in a  $10^{-4}$  water level slope, equal to the channel slope. The analytical solution, using Manning's equation for open channel flow  
312 yields a discharge of  $360 \text{ m}^3/\text{s}$ . The input files for the 5m subgrid version of this model setup can be found in Appendix B1.

313

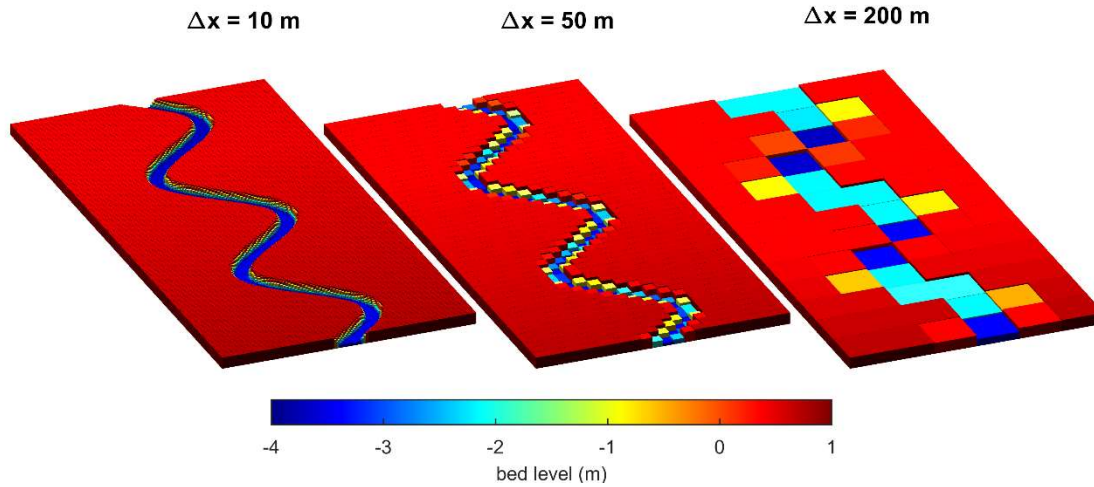
314 The second test is identical to the first, except that it has a meandering channel. The meandering channel has a sinuosity  $\Omega$  of  
315 1.32, i.e. the ratio between the length along the channel (6603 m) and its straight-line length (5000 m) (see e.g. Lazarus and  
316 Constantine, 2013 for background on river sinuosity). As the water levels upstream and downstream of the channel are kept  
317 the same, the water level slope in the meandering channel is smaller by a factor  $\Omega$ , resulting in a (lower) analytical discharge  
318 of  $313 \text{ m}^3/\text{s}$ .



319

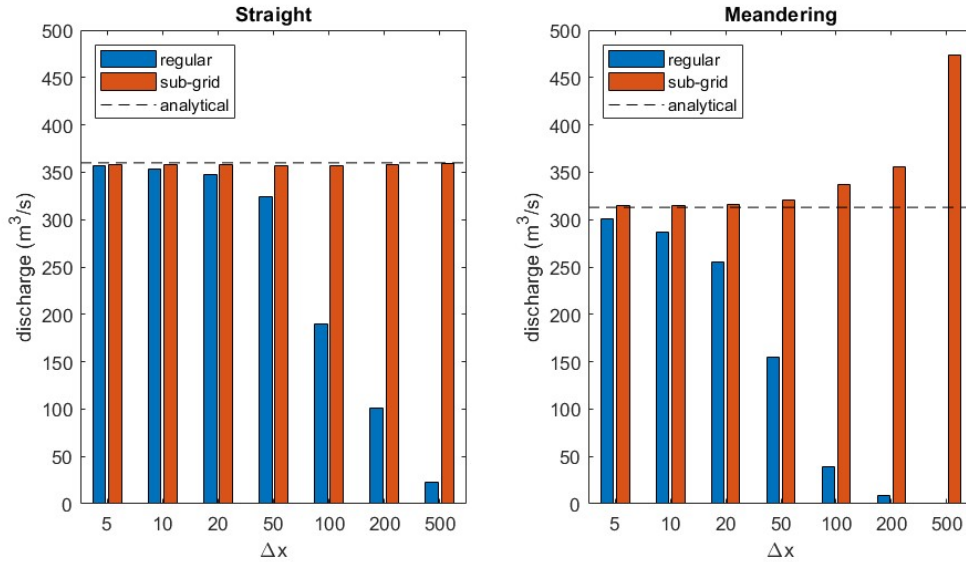
320 **Figure 4. Schematized channel used in the conceptual verification cases, including a straight channel (top view, panel a), a**  
 321 **meandering channel (top view, panel b), and a cross-section (panel c).**

322 Simulations are carried out by SFINCS at various grid resolutions (5, 10, 20, 50, 100, 200, and 500 m), both with and without  
 323 the subgrid corrections. The subgrid simulations use a 1 m resolution subgrid, onto which the DEM is bilinearly interpolated.  
 324 For the regular topography simulations, grid cell averaging is used to schematize the model bathymetry, in which the bed level  
 325 of each cell is set equal to the mean of the DEM pixels within that cell. Figure 5 shows the regular model bathymetry at grid  
 326 resolutions  $\Delta x$  of 10 m, 50 m, and 200 m for the meandering channel. It is clear that whereas the first two capture the channel  
 327 topography reasonably well, the channel depth in the 200 m model is strongly underestimated, and its width is proportionally  
 328 overestimated.



329  
 330 **Figure 5 Schematized meandering channel bathymetry with regular topography for hydraulic grid resolutions  $\Delta x = 10$  m,  $\Delta x = 50$**   
 331 **m, and  $\Delta x = 200$  m**

332 In the first test (straight channel), the regular bathymetry models stay reasonably close to the analytical solution up to  
 333 resolutions of 50m (blue bars in Figure 6 – panel A). The accuracy of the coarser models however degrades significantly with  
 334 decreasing grid resolution as is to be expected. The channel depth in the coarser models is increasingly underestimated, and  
 335 even though its width is proportionately overestimated, the strongly non-linear relationship between water depth and discharge  
 336 results in a decrease of the discharge with decreasing grid resolution. In contrast, the discharges computed by the subgrid  
 337 models are within 2% of the analytical solution across all grid resolutions (red bars in Figure 6 – panel A), proving that, at  
 338 least for very simple conceptual cases, the subgrid corrections presented here are accurate.



339

340 **Figure 6. Effect of grid resolution  $\Delta x$  on computed discharges for regular and subgrid topography in straight (panel a) and**  
 341 **meandering (panel b) channel.**

342 In the second test (meandering channel), the trend of the regular models is similar to those in the first test (blue bars in Figure  
 343 6 – panel B), but the performance is lower than in the straight channel case, with the discharge for the two coarsest regular  
 344 models going to zero. This is caused by the fact that the hydraulic connection between some channel cells is broken in the  
 345 coarsest models (see also Figure 5).

346

347 The subgrid models in the second test show very good accuracy at resolutions up to 50 m. Coarser models start to overestimate  
 348 the discharge. The 500 m model in particular computes a discharge of 473 m³/s (an overestimation of the analytical discharge  
 349 by ~51%). There are two reasons for this: as the coarse mesh does not capture the scale of the meanders, the channel is  
 350 effectively schematized as a straight channel with a length of 5000 m. This leads to an overestimation of the true water level  
 351 slope and resulting wet average flux. Secondly, meanders inside a grid cell result in a larger wet fraction, which the model  
 352 “interprets” as a wide channel, leading to a further overestimation.

353

354 For rivers with meanders that are not resolved by the model grid, we can approximate the discharge overestimation as a function  
 355 of the channel sinuosity:

356

$$\frac{Q_m}{Q_r} = \Omega^{3/2} \quad (27)$$

357 where  $\Omega$  is the sinuosity,  $Q_r$  is the true discharge and  $Q_m$  is the discharge computed with the subgrid corrections (see Appendix  
 358 A for the derivation of Equation 27). Equation 27 suggests that the discharge overestimation in the 500 m subgrid model

359 (which does not resolve the meandering at all) is  $\sim 52\%$  ( $1.32^{3/2}$ ), which closely matches the computed overestimation of  $\sim 51\%$   
360 reported earlier.

## 361 **4 Real-world application cases**

### 362 **4.1 Tidal propagation St. Johns River**

363 Leijnse et al. (2021) described SFINCS model results for Hurricane Irma (2017) along the St. Johns River (Florida, USA). The  
364 length of the river is about 170 kilometers from its mouth to Lake George upstream (Figure 7 – panel A) where still a small  
365 tidal signal remains. Its width varies between 400 m and 5 km. Although the model showed good skill when compared to a  
366 full-physics Delft3D model, its 100-meter grid resolution proved insufficient to adequately propagate the tide into the estuary.  
367

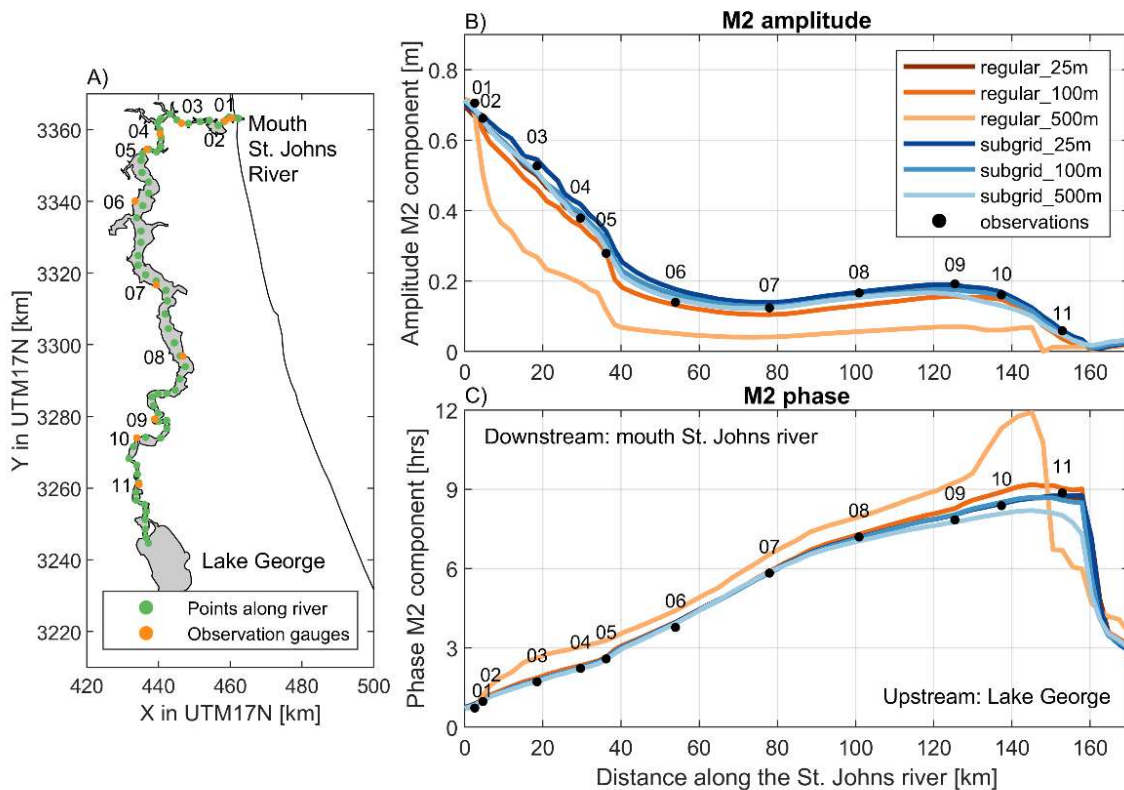
368 In this test case, the St. Johns River SFINCS model from Leijnse et al. (2021) is adapted and tidal propagation into the river is  
369 simulated at several horizontal resolutions (25, 50, 100, 200, and 500 m) using both the regular and subgrid version of SFINCS.  
370 The topography and bathymetry data are improved by using data obtained from the Continuously Updated Digital Elevation  
371 Model (CUDEM; CIRES, 2014). The Manning friction coefficient in the river is set to  $0.02 \text{ s/m}^{1/3}$ . The offshore boundary  
372 water levels are derived from TPXO 8.0 tidal components (Egbert and Erofeeva, 2002). Computed water levels are validated  
373 against observed tidal components from 11 tide stations (retrieved through Delft Dashboard; van Ormondt et al., 2020) (Figure  
374 7 – panel A). The input files for the 25m subgrid version of this model setup can be found in Appendix B2. Values for the  
375 subgrid corrections are stored in a table with 20 discrete vertical levels.

376  
377 Simulations are carried out over a one-month period to assess the model's capability to propagate the tide into the river.  
378 Analysis of the main tidal component M2 across different model variations reveals considerable differences in the upstream  
379 propagation (Figure 7B). The amplitude of M2 is approximately 75 cm at the offshore boundary and sharply decreases near  
380 the city of Jacksonville, where the river narrows significantly (about 40 kilometers upstream along the river). At 100-meter  
381 resolution, the SFINCS model with regular topography can reproduce the main trends but underestimates the tidal amplitudes  
382 relative to observations (Figure 7B), as in Leijnse et al. (2021). At the coarser 500-meter resolution, this underestimation of  
383 amplitude is significantly stronger and the tide arrives too late (Figure 7C). The tidal propagation only accurately matches the  
384 observations when utilizing a 25-meter resolution with the regular topography.

385  
386 The subgrid version of SFINCS, on the same 100-meter grid resolution, mitigates the underestimation of the regular (non-  
387 subgrid) version (Figure 7B). The median error of M2 amplitude prediction over the 11 observation stations decreases from  
388 2.6 cm to 0.4 cm, the phase error from 4.1 to 2.1 degrees, and the overall RMSE from 8.0 to 6.4 cm. Further analysis with  
389 different grid resolutions illustrates that the model that uses subgrid corrections propagates the tide inland properly, even at



390 very coarse resolutions of 500 meters. The tidal phasing is also generally more accurately resolved when applying subgrid  
 391 corrections. The RMSE of the computed M2 amplitude over a one-month tidal prediction increases from about 8 cm to about  
 392 20 cm for coarser grid resolutions in regular bathymetry mode. However, when incorporating subgrid corrections it remains  
 393 stable at around 8 cm. While high tide predictions remain accurate for the model with subgrid corrections at lower grid  
 394 resolutions (Table 1), the performance decreases more significantly for low water, indicating that during these periods, the low  
 395 tide flushing of the river may be underestimated. Including the subgrid raises computational costs by around 28-58% (37%  
 396 on average) as a result of the extra overhead involved in querying the subgrid tables. A comparison between the 25-meter  
 397 regular resolution and the 100-meter subgrid resolution demonstrates similar skill but reveals a factor 50 speed-up, allowing  
 398 the subgrid version to use coarser model resolutions with significantly lower computational costs without sacrificing precision.



399  
 400 **Figure 7. Overview of the St. Johns River near Jacksonville, FL, USA (Panel A), with analysis points (green dots) and tide gauges**  
 401 **(yellow dots). Panel B: Observed (black dots) and modeled (colors) M2 tidal amplitudes along the river from downstream to**  
 402 **upstream. Panel C: Observed (black dots) and modeled (colors) M2 tidal phases along the river. Different colors represent variations**  
 403 **in the SFINCS model setup: red indicates the regular non-subgrid version, while blue denotes the subgrid version, with decreasing**  
 404 **color intensity indicating a decrease in model resolution. M2 phase is converted from degrees to hours, assuming one degree equals**  
 405 **12.42 hours / 360 degrees. The coordinate system is WGS 84 / UTM 15 N (EPSG 32615).**

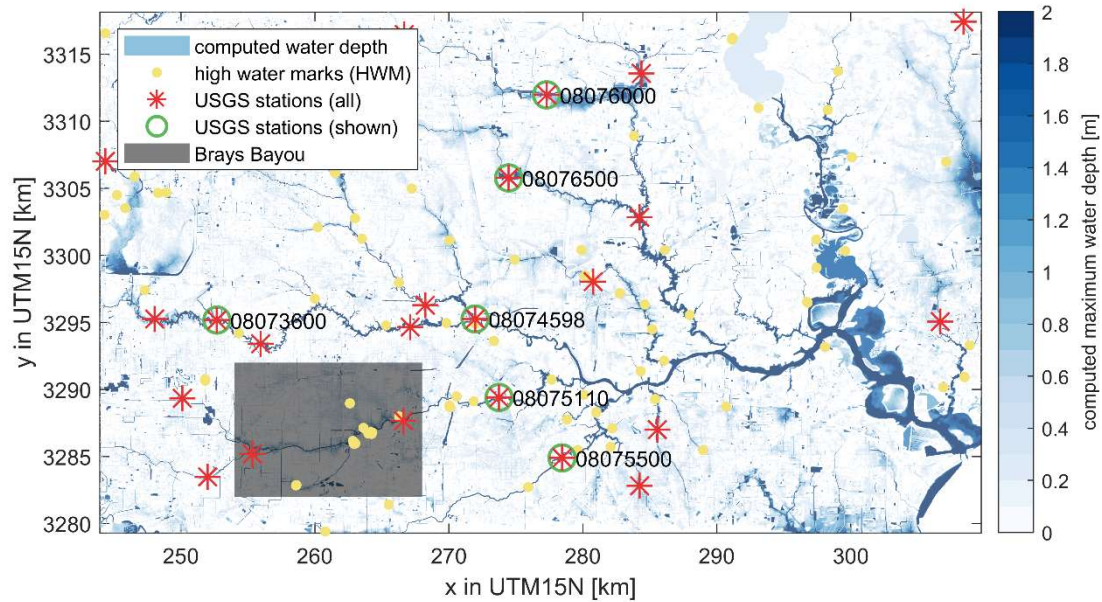
406 **Table 1. Overview of model skill and computational expense for evaluated scenarios of inland tidal propagation at the St. Johns**  
 407 **River, FL. Metrics include RMSE of overall difference in time-series compared to observations, RMSE of high water peaks, RMSE**  
 408 **of low water peaks, difference in M2 amplitude, and difference in M2 phase, all presented as medians over 11 observation stations.**  
 409 **The last column shows the runtime in seconds, measured on an Intel Core i9-10980XE CPU. Each simulation was run three times,**  
 410 **and the minimum runtime was recorded to eliminate potential contamination of timing. Additionally, the relative error to the regular**  
 411 **25m configuration has been computed for the overall RMSE to provide further insight into the performance of the subgrid version**  
 412 **of SFINCS compared to the baseline model. We also computed the percentage increase in computational costs for the subgrid**  
 413 **version, which is reflected in the model runtime column to illustrate the additional computational expense.**

Run	RMSE overall [cm]	RMSE high water [cm]	RMSE low water [cm]	Amplitude difference M2 [cm]	Phase difference M2 [°]	Model runtime [sec]
regular_25m	7.7 (100%)	6.6	9.1	-0.3	1.0	68348
regular_50m	7.8 (101%)	5.7	10.1	-1.7	5.0	8273
regular_100m	8.0 (104%)	4.3	12.5	-2.6	4.1	854
regular_200m	12.0 (156%)	5.3	19.5	-6.7	6.5	139
regular_500m	16.1 (209%)	8.3	25.4	-10.9	21.4	29
subgrid_25m	8.7 (113%)	8.3	7.3	1.5	1.2	87652 (128%)
subgrid_50m	7.5 (97%)	7.6	6.1	0.6	1.5	11510 (139%)
subgrid_100m	6.4 (83%)	5.3	6.1	-0.4	2.1	1344 (158%)
subgrid_200m	7.8 (101%)	7.3	8.2	-1.0	1.5	182 (130%)
subgrid_500m	8.2 (106%)	6.6	8.7	-0.3	-1.5	30 (132%)

414

415 **4.2 Pluvial flooding during Hurricane Harvey**

416 Sebastian et al. (2021) used SFINCS to hindcast the flood extent and flood depth during Hurricane Harvey (2017) in Houston,  
417 TX. The model was validated against water level time series at 21 United States Geological Survey (USGS) observation points  
418 and 115 high water mark (HWM) locations (Figure 8). The original model was run with a regular 25-meter resolution grid  
419 based on a high-resolution continuous topo-bathymetry across the area of interest. The model was compared to observed data  
420 across the study area, achieving an average error of 73 cm.



421  
422 **Figure 8. Modeled flood inundation in the urban areas of Houston, TX, simulated with SFINCS at a 25m resolution with subgrid**  
423 **corrections. Water depths less than 0.10 m are excluded for clarity. USGS stream gauges (red stars) and high-water marks (HWMs,**  
424 **yellow circles) used for model validation are shown as solid circles. Six USGS stations, presented as time series in Figure 9, are**  
425 **marked with green circles, including their station numbers. A zoom-in of the midstream portion of Brays Bayou is shown in Figure**  
426 **10. The coordinate system is WGS 84 / UTM 15 N (EPSG 32615). © Microsoft.**

427 In this field case, the model setup is adapted and flooding across Houston is simulated at several horizontal resolutions. In  
428 particular, three variations for regular SFINCS (25, 50, and 100 meters) and 5 variations of subgrid (same resolutions as regular  
429 mode, including 200, and 500 meters) were created. Model settings were based on the Sebastian et al. (2021) model except for  
430 the model resolution. Friction and infiltration capacity were cell-averaged from the original setup for the coarser model runs.  
431 The input files for the 25m subgrid version of this model setup can be found in Appendix B3. In the subgrid version, we  
432 included a higher than typical 100 discrete vertical levels to describe the subgrid quantities since during testing model skill  
433 improved when including more vertical levels.

434

435 Almost all model versions reproduce the general shape of the observed hydrograph. However, the coarser regular version of  
 436 SFINCS results in larger errors mainly due to an overestimation of the water level (Figure 9). The overestimation is driven by  
 437 an incorrect representation of the bed level which is averaged across larger areas and can therefore not depict the local bayous  
 438 with coarser grid cells. SFINCS with the subgrid corrections improves the model skill (Table 2). For example, when comparing  
 439 the 25-meter regular with the subgrid version on the same computational resolution, the Nash-Sutcliffe Efficiency(NSE<sup>1</sup>)  
 440 increases from 0.35 to 0.58. NSE is a statistical metric used to evaluate the predictive accuracy of models by comparing  
 441 observed and predicted values. NSE values range from 0 to 1, with values closer to 1 indicating a better-performing model.  
 442 An NSE value of 0 means the model's predictions are as accurate as using the mean of the observed data as the predictor.  
 443 Model skill increases because more topo-bathymetry information is considered per grid cell via the subgrid correction in the  
 444 momentum and continuity equations (see Sections 2.2 and 2.3). Despite the subgrid correction, model skill still decreases with  
 445 decreasing computational resolution. For example, a 500-meter simulation with subgrid correction has an NSE close to zero.  
 446 Including the subgrid feature increases computational expense by 87 to 175 % (average of 128%), because of additional  
 447 overhead in querying the subgrid tables. The highest model skill is obtained with the finest resolution (25m used here) including  
 448 subgrid corrections.

449

450 SFINCS can store the maximum computed water level across the computational domain, with the capability to downscale this  
 451 data to higher-resolution flood maps as part of a post-processing step. In particular, to calculate flood depths at the DEM scale,  
 452 the elevation of individual DEM pixels is subtracted from the corresponding cell's water level (see Section 2.4). For instance,  
 453 the results demonstrate that the 25-meter resolution outcomes and those downscaled to a 100-meter subgrid are quite similar.  
 454 This is illustrated in Figure 10, which shows modeled flood inundation in the midstream portion of Brays Bayou using four  
 455 different SFINCS model options. Panels A and C in Figure 10 highlight the comparison: Panel A presents the regular 25-meter  
 456 resolution, while Panel C depicts the 'subgrid 100m – downscaled' method, which applies a downscaling method to the DEM  
 457 resolution as a post-processing step. However, the 100-meter subgrid resolution runs 35 times faster than the 25-meter regular  
 458 SFINCS version, while maintaining a similar level of accuracy (see Table 2) and thus, producing comparable extents of  
 459 flooding. Nonetheless, it is important to note that the 100-meter resolution results tend to provide a coarser visual representation  
 460 of flood extents, often overestimating them (see panels B and D in Figure A1) for both the regular and subgrid models.

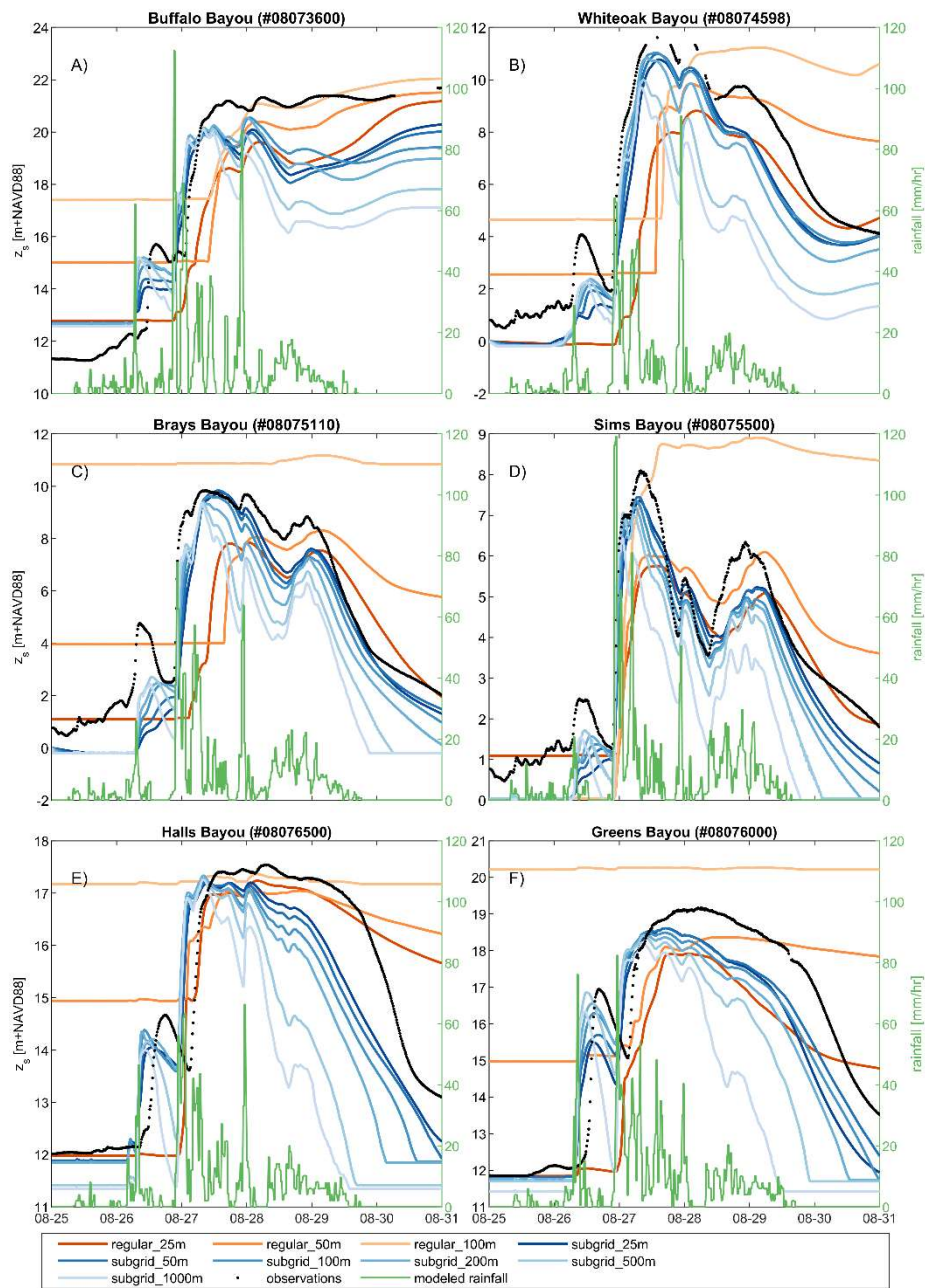
461

---

<sup>1</sup>  $NSE = 1 - \frac{\sum_{i=1}^n (O_i - P_i)^2}{\sum_{i=1}^n (O_i - \bar{O})^2}$  where O is *i*th observed value, P<sub>i</sub> is *i*th predicted value and  $\bar{O}$  is the mean of the observed data

462 **Table 2. Overview of model skill and computational expense for evaluated scenarios of pluvial flooding during Harvey. Model skill**  
 463 **metrics for time series, including NSE (Nash-Sutcliffe Efficiency), MAE (Mean Absolute Error), RMSE (Root Mean Square Error),**  
 464 **and bias, as well as MAE for high-water marks (HWMs). The last column shows the runtime in seconds, measured on an Intel Core**  
 465 **i9-10980XE CPU. Each simulation was run three times, and the minimum runtime was recorded to eliminate potential**  
 466 **contamination of timing on Windows. Additionally, the relative MAE to the regular model configuration has been computed to**  
 467 **provide further insight into the performance improvements with the subgrid corrections. We also computed the percentage increase**  
 468 **in computational costs for the subgrid version, which is reflected in the model runtime column to illustrate the additional**  
 469 **computational expense.**

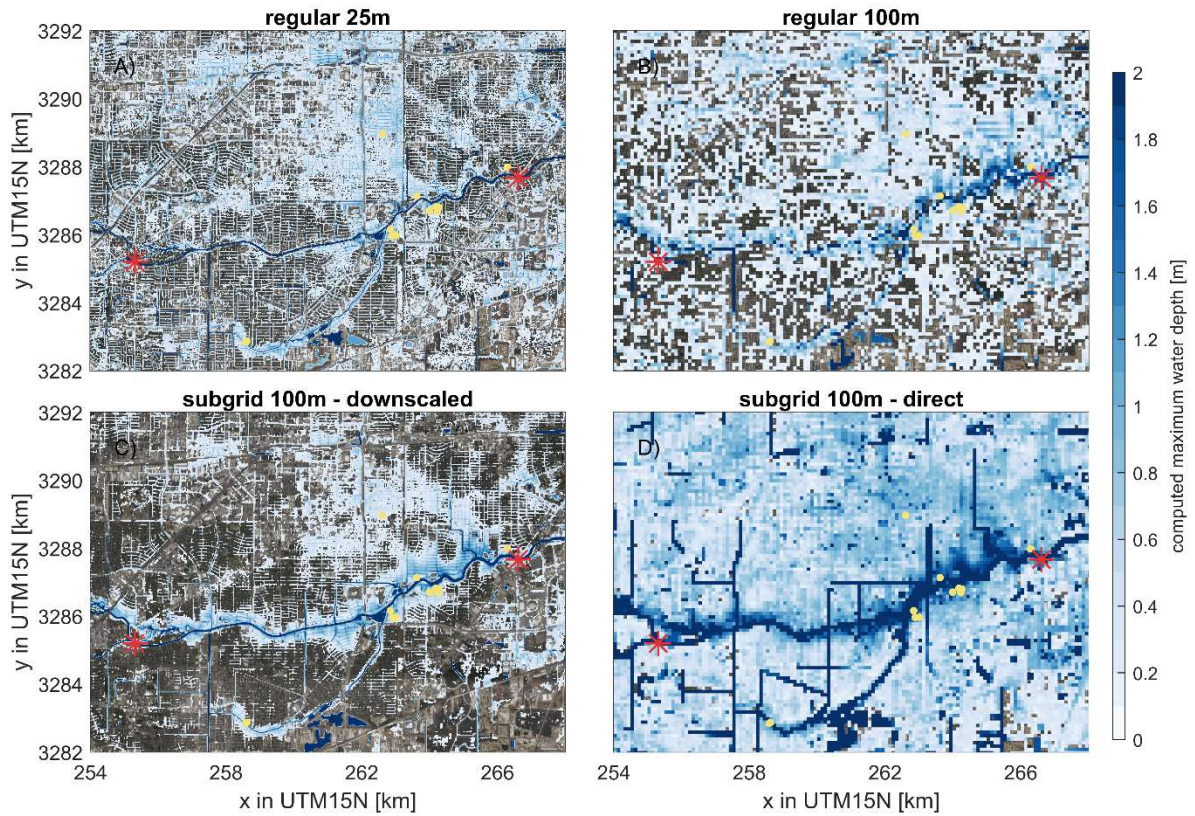
	Time series				HWM	
simulation	NSE [-]	MAE [m]	RMSE [m]	bias [m]	MAE [m]	Model runtime [sec]
regular_25m	0.349	1.68 (100%)	2.14	-0.548	0.73	11197
regular_50m	-0.007	2.08 (124%)	2.58	0.405	0.68	1258
regular_100m	-1.988	3.41 (203%)	3.94	2.493	0.84	118
subgrid_25m	0.581	1.29 (77%)	1.58	-0.842	0.89	20951 (187%)
subgrid_50m	0.540	1.30 (77%)	1.57	-0.963	0.94	2800 (223%)
subgrid_100m	0.495	1.35 (80%)	1.62	-0.984	0.98	324 (275%)
subgrid_200m	0.310	1.62 (96%)	1.94	-1.226	1.09	38
subgrid_500m	0.011	2.05 (122%)	2.47	-1.671	1.27	7



470

471 **Figure 9. Overview of (computed) water levels during Hurricane Harvey. Comparison between modeled (colored lines) and observed**  
 472 **(black lines) hydrographs at six USGS gauge locations (labeled in Figure 8): Panels A. Buffalo Bayou (USGS 08073600); B. White**  
 473 **Oak Bayou at Main Street (USGS 08074598); C. Brays Bayou at MLK Jr. Blvd (USGS 08075110); D. Sims Bayou at Houston, TX**  
 474 **(USGS 08075500); E. Vince Bayou at Pasadena, TX (USGS 08075730); f Greens Bayou nr Houston, TX (USGS 08076000). Different**  
 475 **colors represent variations in the SFINCS model setup. Red is used for the regular version of SFINCS (non-subgrid). Blue is used**

476 for the subgrid version of SFINCS. Decreasing color intensity depicts a decrease in model resolution. Rainfall intensity is included  
477 as the green line and uses the right y-axis.



478  
479 **Figure 10. Modeled flood inundation in the midstream portion of Brays Bayou for 4 different SFINCS model options: A) regular**  
480 **25m, b) regular 100m, c) ‘subgrid 100m – downscaled’ is using the same model simulation as ‘subgrid 100m – direct’ (panel D), but**  
481 **then applying a downscaling method to the DEM resolution as a post-processing step. Water depths less than 0.10 m have been**  
482 **excluded for visual purposes. The locations of USGS stream gauges (red stars) and HWMs (yellow circles) used for the model**  
483 **validation are shown. The coordinate system of this figure is WGS 84 / UTM 15 N (EPSG 32615). © Microsoft.**

484

## 485 5 Discussion

486 The integration of subgrid corrections into SFINCS has led to significant enhancements in accuracy, as evidenced in both  
487 conceptual verification cases (Section 3) and real-world scenarios, including tidal propagation (Section 4.1) and pluvial  
488 flooding (Section 4.2). This section delves into the impact of these accuracy enhancements and outlines the remaining  
489 challenges and areas for future research, particularly concerning flow-blocking features and the overestimation of fluxes in  
490 meandering systems.

491

492 The ability to achieve improved accuracy on the same grid resolution signifies progress. However, in practical terms, a more  
493 accurate simulation also allows for the use of coarser model resolutions. This is particularly advantageous given SFINCS's  
494 explicit numerical scheme, enabling faster and thus more efficient compound flood modeling. For example, in the real-world  
495 application cases of tidal propagation (Section 4.1) and pluvial flooding (Section 4.2), a subgrid model at 100-meter resolution  
496 demonstrates comparable, if not higher, performance to the regular 25-meter resolution SFINCS model. However, the  
497 computational cost is significantly lower with a factor of 35-50 speedup. The introduction of subgrid corrections does introduce  
498 additional computational expenses versus regular SFINCS for the same grid spacing. In the St. Johns River case (Section 4.1),  
499 where we used 20 discrete bins to describe the subgrid quantities, the increase in computational costs was relatively low with  
500 an average increase of 37% when comparing the same grid spacing. In contrast, higher costs were observed in the Hurricane  
501 Harvey case (Section 4.2), where model performance improved when 100 discrete bins were used instead of the more typical  
502 20 bins, leading to an average computational cost increase of 128%. Therefore, the increase in computational costs is dependent  
503 on the number of bins used to describe the subgrid quantities, with finer binning sometimes providing better accuracy at the  
504 cost of increased computational demands. Additionally, using more bins also results in larger NetCDF subgrid files. For  
505 example, in the 200-meter Harvey case, the subgrid file size was 343 MB, compared to 65 MB for the 200-meter Jacksonville  
506 case, a nearly fivefold increase. Notably, the number of active cells was twice as large for the Jacksonville case, which  
507 demonstrates that subgrid file sizes scale linearly as a function of both the number of active cells and the number of discrete  
508 bins.

509

510 The downscaling routines implemented also allowed for the use of the high-resolution data in the post-processing step.  
511 However, the simple subtraction of the computed water level and high-resolution topography (introduced in Section 2.4 and  
512 applied in Section 4.2) might result in water in an area that would not be flooded using high-resolution models. While this  
513 might not affect the accuracy compared to water level stations, it does influence results and flood extents. In particular,  
514 disconnected grid cells might pop up behind levees and other flow-breaking features which form a challenge when  
515 communicating the results to stakeholders. Moreover, the presented downscaling routine has limited use for areas with steep  
516 gradients where the assumption of a constant water level per computational cell is invalid. Therefore, exploring more  
517 sophisticated hybrid surrogate models might improve the dynamic evolution of the flood extent (Fraehr et al., 2022).



518 Furthermore, in the subgrid SFINCS model, we currently estimate infiltration rates on the computational grid. This approach  
519 does not account for higher-resolution information in the estimation of infiltration rates, which may lead to less accurate  
520 representations of infiltration rates in areas these vary significantly at the subgrid scale. Future work could explore  
521 integrating finer-scale soil, and topographic data into the infiltration estimation process to further enhance the model's  
522 performance, particularly in regions with partial wet cells and heterogeneous soil properties.

523

524 It is important to note that the real-world cases evaluated here are not without limitations. One ongoing challenge for the  
525 modeling community is the insufficient representation of river bathymetry in combined topo-bathymetry datasets. In many  
526 cases, river bathymetry is not well captured, which can affect the accuracy of hydrodynamic models, particularly for riverine  
527 flooding. Furthermore, land cover maps used to estimate bed friction can introduce contamination where land roughness is  
528 mapped onto the river and therefore affecting model accuracy. No specific adjustments were made to the real-world cases  
529 presented in this paper, and the published models were simply adjusted to be run at several resolutions with and without subgrid  
530 corrections.

531

532 Addressing subgrid connectivity poses a significant challenge for the implementation described in this paper and the broader  
533 modeling community. In contrast to approaches that relied on cell and edge clones (Casulli, 2009b; Begmohammadi et al.,  
534 2021) or artificial diffusion (Rong et al., 2023), SFINCS employs a subgrid weir formulation. This formulation, which is  
535 aligned with (or snapped to) the grid, controls the flow between two cells but requires the creation of subgrid features during  
536 a pre-processing phase. To date, these features have been manually identified. However, there is ongoing research into  
537 algorithms capable of detecting flow-blocking features as well as the integration of methods from existing literature or direct  
538 modifications to the subgrid lookup tables to account for this. In scenarios where flow-blocking features (such as levees or  
539 urban structures) are not adequately captured, the model may underestimate the extent of localized flooding.

540

541 Similarly, the overestimation of fluxes in situations with unresolved meanders continues to be a challenge. This issue is not  
542 exclusive to SFINCS's implementation of subgrid corrections but is a common challenge across subgrid modeling. Various  
543 estimates for the sinuosity  $\Omega$  have been reported in scientific literature. Lazarus and Constantine (2013) suggest that the typical  
544 range for  $\Omega$  lies between 1 and 3, where 1 corresponds to a straight channel and 3 represents the upper limit for natural, freely  
545 migrating meandering rivers. Hence, when using a computational grid that does not resolve the river meanders, the presented  
546 subgrid corrections may overestimate discharges by more than a factor of 5 (or  $3^{3/2}$ ). This is especially important in real-world  
547 scenarios involving highly sinuous river systems, where discharge inaccuracies can significantly affect flood predictions. To  
548 mitigate this, it is recommended that the grid spacing of the computational grid does not exceed the width of the river channel.

549 **6 Conclusions**

550 Large-scale flood models require high accuracy at acceptable computational times. One strategy to achieve this is to use  
551 information available at a higher resolution than the hydrodynamic grid resolution in models through subgrid corrections. This  
552 paper describes a set of subgrid corrections to the Linear Inertial Equations (LIE) using grid average quantities (depth,  
553 representative roughness, wet fraction, and flux to the momentum equations and for the wet volume in the continuity equation)  
554 which were implemented in SFINCS. The model uses pre-processed subgrid tables that correlate water levels with  
555 hydrodynamic quantities by assuming constant water levels for all subgrid pixels.

556  
557 The conceptual case of a straight channel showed good skill in terms of discharge fluxes with the subgrid model regardless of  
558 the model resolution while the accuracy of the regular models without subgrid correction decreased significantly with  
559 decreasing resolution. For the meandering channel, differences start to emerge for coarser model resolutions with and without  
560 subgrid corrections. In particular, the difference in discharge estimation was overestimated by 50% for the coarsest subgrid  
561 model used. The ratio between the length along the channel and its straight-line length (also known as sinuosity or  $\Omega$ ) served  
562 as a valuable metric for quantifying flux overestimations. The conceptual cases gave confidence that the corrections were  
563 correctly implemented while also highlighting their limitations in grids that do not adequately resolve river meanders. In  
564 particular, we introduced an equation that allows for approximation of the discharge overestimation as a function of the channel  
565 sinuosity:

566  
567 Real-world application cases further validated the benefits of subgrid corrections. For tidal propagation in the St. Johns River,  
568 the subgrid model with a 500-meter resolution matched the accuracy of the 25-meter standard SFINCS model. Similarly, in  
569 modeling pluvial flooding during Hurricane Harvey, a 25-meter resolution SFINCS model was necessary to achieve a Nash–  
570 Sutcliffe Efficiency (NSE) of 0.35, while the subgrid variant at the same resolution outperformed this with an NSE of 0.58  
571 (where a score of 1 would be perfect) and maintained comparable accuracy even at a coarser 100-meter resolution. Although  
572 subgrid corrections introduce additional computational costs—ranging from 37% to 128% depending on binning density—  
573 they provide significant benefits in performance and accuracy, achieving a factor of 35-50 speedup by enabling the use of  
574 coarser resolutions and thus improving efficiency in real-world flood modeling applications.

575  
576 Building on these findings, the implementation of subgrid corrections for LIE within SFINCS demonstrates significant  
577 potential for improving accuracy and reducing computational demands in compound flooding simulations. However, the  
578 broader relevance of subgrid corrections should not be limited to LIE or SFINCS alone. Subgrid corrections could benefit a  
579 wide range of hydrodynamic models, such as full-physics or reduced-complexity models alike. Furthermore, these corrections  
580 could be applied across diverse environmental conditions, including urban pluvial flooding, coastal storm surge, and riverine  
581 flooding, thereby enhancing the generalizability and utility of hydrodynamic modeling across various domains. Overall, the

582 results from both conceptual and real-world cases show that subgrid corrections are a valuable addition to hydrodynamic  
583 modeling, particularly when balancing the need for accuracy with computational efficiency.

584

585 *Code and data availability.*

586 The SFINCS code is freely available to anyone and published on Zenodo (<https://zenodo.org/doi/10.5281/zenodo.8038533>)  
587 and GitHub (<https://github.com/Deltares/SFINCS>).

588

589 *Author contributions.*

590 MO is the primary developer of the SFINCS model. KN, RG, and TL have actively contributed to the development of the  
591 model. AvD initiated and co-wrote this paper. All authors were actively involved in the interpretation of the model outcomes  
592 and the writing process.

593

594 *Competing interests.*

595 The authors declare that they have no conflict of interest.

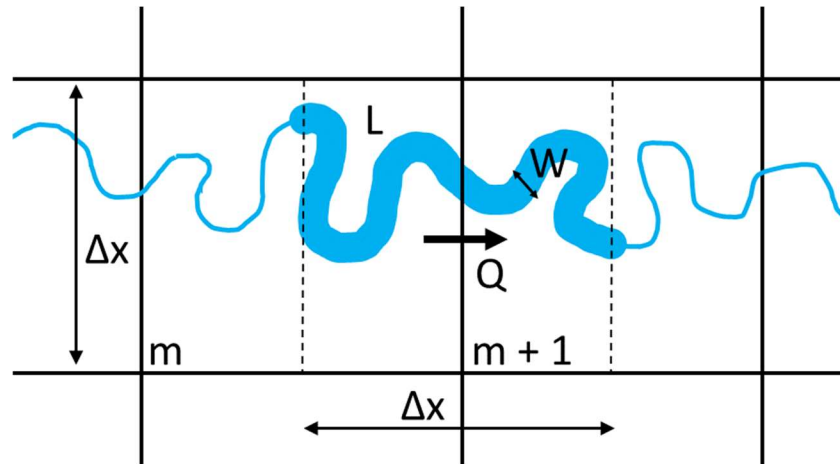
596

597 *Acknowledgments and financial support*

598 We acknowledge the Deltares SITO-IS research funding under Moonshot 2 – Flooding, which has provided funding to develop  
599 the model and write this paper.

## 601 Appendix A: Derivation of discharge overestimation due to unresolved meandering

602 The subgrid corrections presented in this paper may result in an overestimation of fluxes between grid cells in places where  
 603 river meanders are not sufficiently resolved by the computational grid. The overestimation may be expressed as the ratio  
 604 between the computed and theoretical fluxes. In this appendix, we describe a simple relation between this ratio and the river  
 605 sinuosity in cases where the model grid does not resolve the meanders at all. The sinuosity is defined as the ratio between the  
 606 length along the channel and its straight-line length (e.g. Lazarus and Constantine, 2013).



607

608 **Figure A1. Conceptual figure of the sinuosity which is defined as the ratio between the length along the channel and its straight-**  
 609 **line length**

610 Using Manning's formula, the theoretical discharge can be described with:

$$611 \quad Q_r = \frac{W \sqrt{\frac{\Delta z}{L}} H^{5/3}}{n} \quad (A.1)$$

612 where  $W$  is the river width,  $L$  is the length of the center line of river stretch,  $\Delta z$  is the water level difference over the river  
 613 stretch,  $H$  is the channel depth (assumed uniform), and  $n$  is the Manning's roughness coefficient.

614 Inside a model using the subgrid corrections, the discharge computed at the cell interface will be:

$$615 \quad Q_m = \Delta x \frac{\varphi \sqrt{\frac{\Delta z}{\Delta x}} H^{5/3}}{n} \quad (A.2)$$

616 where  $\Delta x$  is the grid size,  $\varphi$  is the wet fraction of the velocity point, and  $H$  is the "wet-average" depth.

617 We assume here that the sinuosity is:

$$618 \quad \Omega = \frac{L}{\Delta x} \quad (A.3)$$

619 Furthermore, the wet fraction  $\varphi$  in A.2 can be written defined as the river area  $W \times L$  divided by the cell area:

620 
$$\varphi = \frac{WL}{\Delta x^2} = \frac{W}{\Delta x} \Omega \quad (A.4)$$

621 After substituting  $\varphi$  in Eq. A.2 with Eq. A.4, we can write the overestimation (i.e. the ratio of the computed and theoretical  
 622 discharge  $Q_m / Q_r$ ) as:

623 
$$\frac{Q_m}{Q_r} = \frac{\Delta x \frac{W}{\Delta x} \Omega \frac{\sqrt{\frac{\Delta z}{\Delta x}} H^{5/3}}{n}}{W \frac{\sqrt{\frac{\Delta z}{L}} H^{5/3}}{n}} = \Omega \sqrt{\frac{L}{\Delta x}} = \Omega \sqrt{\Omega} = \Omega^{3/2} \quad (A.5)$$

624 **Appendix B: Input files for cases considered in this manuscript**

625 **Conceptual verification cases: straight and meandering channels**

626 mmax = 11  
627 nmax = 26  
628 dx = 200  
629 dy = 200  
630 x0 = -1000  
631 y0 = 0  
632 rotation = 0  
633 tref = 20190101 000000  
634 tstart = 20190101 000000  
635 tstop = 20190103 000000  
636 tspinup = 60  
637 dtout = 3600  
638 dthisout = 600  
639 dtmaxout = 3600  
640 alpha = 0.5  
641 theta = 0.95  
642 huthresh = 0.005  
643 zsini = 1  
644 qinf = 0  
645 rhoa = 1.25  
646 rhow = 1024  
647 advection = 1  
648 depfile = sfincs.dep  
649 mskfile = sfincs.msk  
650 indexfile = sfincs.ind  
651 bndfile = sfincs.bnd  
652 bzsfile = sfincs.bzs  
653 srcfile = sfincs.src  
654 disfile = sfincs.dis  
655 sbgfile = sfincs\_subgrid.nc?  
656 obsfile = sfincs.obs  
657 crsfile = sfincs.crs  
658 manningfile = sfincs.manning  
659 inputformat = bin  
660 outputformat = net  
661 storevelocity = 1  
662 storevel = 1

663 **Tidal propagation St. Johns River**

664 mmax = 2720  
665 nmax = 5520  
666 dx = 25  
667 dy = 25  
668 x0 = 459437.0  
669 y0 = 3375791.0

670 rotation = -164.0  
671 epsg = 32617  
672 latitude = 0.0  
673 tref = 20180901 000000  
674 tstart = 20180901 000000  
675 tstop = 20180931 000000  
676 tspinup = 60.0  
677 dtout = 86400  
678 dthisout = 600.0  
679 dtmaxout = 9999999999  
680 trstout = -999.0  
681 alpha = 0.5  
682 theta = 1.0  
683 huthresh = 0.01  
684 manning\_land = 0.04  
685 manning\_sea = 0.02  
686 rgh\_lev\_land = 0.0  
687 zsini = 0.0  
688 qinf = 0.0  
689 rhoa = 1.25  
690 rhow = 1024.0  
691 advection = 1  
692 btfiler = 60.0  
693 viscosity = 1  
694 depfile = sfincs.dep  
695 mskfile = sfincs.msk  
696 indexfile = sfincs.ind  
697 bndfile = .sfincs.bnd  
698 bzsfile = sfincs.bzs  
699 sbgfile = sfincs\_subgrid.nc  
700 obsfile = noaa\_xtide\_v4\_added\_debug\_points.obs  
701 inputformat = bin  
702 outputformat = net

703 **Pluvial flooding during Hurricane Harvey**

704 mmax = 2632  
705 nmax = 1555  
706 dx = 25  
707 dy = 25  
708 x0 = 243943.538  
709 y0 = 3279280.3807  
710 rotation = 0  
711 epsg = 32615  
712 tref = 20170825 000000  
713 tstart = 20170825 000000  
714 tstop = 20170831 000000  
715 dtout = 86400  
716 dthisout = 600  
717 dtmaxout = 518400

718 dtwnd = 600  
719 alpha = 0.5  
720 theta = 1  
721 huthresh = 0.05  
722 rgh\_lev\_land = 0  
723 zsini = 0  
724 qinf = 0  
725 rhoa = 1.25  
726 rhow = 1000  
727 advection = 1  
728 depfile = sfincs.dep  
729 mskfile = sfincs.msk  
730 indexfile = sfincs.ind  
731 bndfile = sfincs.bnd  
732 bzsfile = sfincs.bzs  
733 srcfile = sfincs.src  
734 disfile = sfincs.dis  
735 sbgfile = sfincs\_subgrid.nc  
736 amprfile = Observations\_Interpolate\_600x600\_halfhour\_test.ampr  
737 obsfile = sfincs.obs  
738 inputformat = bin  
739 outputformat = net  
740 qinffile = qinf\_constanttime\_spatialvary  
741 storevel = 1



742 **References**

- 743 Bates, P. D., Horritt, M. S., & Fewtrell, T. J. (2010). A simple inertial formulation of the shallow water equations for efficient  
744 two-dimensional flood inundation modelling. *Journal of Hydrology*, 387(1–2), 33–45.  
745 <https://doi.org/10.1016/j.jhydrol.2010.03.027>
- 746 Begmohammadi, A., Wirasaet, D., Poisson, A., Woodruff, J. L., Dietrich, J. C., Bolster, D., & Kennedy, A. B. (2023).  
747 Numerical extensions to incorporate subgrid corrections in an established storm surge model. *Coastal Engineering*  
748 *Journal*, 65(2), 175–197. <https://doi.org/10.1080/21664250.2022.2159290>
- 749 Begmohammadi, A., Wirasaet, D., Silver, Z., Bolster, D., Kennedy, A. B., & Dietrich, J. C. (2021). Subgrid surface  
750 connectivity for storm surge modeling. *Advances in Water Resources*, 153, 103939.  
751 <https://doi.org/10.1016/j.advwatres.2021.103939>
- 752 Begmohammadi, A., Wirasaet, D., Lin, N., Dietrich, J. C., Bolster, D., & Kennedy, A. B. (2024). Subgrid modeling for  
753 compound flooding in coastal systems. *Coastal Engineering Journal*, 66(3), 434–451.  
754 <https://doi.org/10.1080/21664250.2024.2373482>
- 755 Brunner, G. (2016). HEC-RAS River Analysis System Version 5.0—Hydraulic Reference Manual. Hydrologic Engineering  
756 Center, Davis, California, US.
- 757 Casulli, V. (2009a). A high-resolution wetting and drying algorithm for free-surface hydrodynamics. *International Journal for*  
758 *Numerical Methods in Fluids*, 60(4), 391–408. <https://doi.org/10.1002/flid.1896>
- 759 Casulli, V. (2019b). Computational grid, subgrid, and pixels. *International Journal for Numerical Methods in Fluids*, 90(3),  
760 140–155. <https://doi.org/10.1002/flid.4715>
- 761 CIRES. (2014). Cooperative Institute for Research in Environmental Sciences (CIRES) at the University of Colorado, Boulder.  
762 2014: Continuously Updated Digital Elevation Model (CUDEM). Accessed 6/30/21. <https://doi.org/10.25921/ds9v-ky35>
- 763 Defina, A. (2000). Two-dimensional shallow flow equations for partially dry areas. *Water Resources Research*, 36(11), 3251–  
764 3264. <https://doi.org/10.1029/2000WR900167>
- 765 Didier, D., Caulet, C., Bandet, M., Bernatchez, P., Dumont, D., Augereau, E., Floc’h, F., & Delacourt, C. (2020). Wave runup  
766 parameterization for sandy, gravel and platform beaches in a fetch-limited, large estuarine system. *Continental Shelf*  
767 *Research*, 192, 104024. <https://doi.org/10.1016/j.csr.2019.104024>
- 768 Egbert, G. D., & Erofeeva, S. Y. (2002). Efficient inverse modeling of barotropic ocean tides. *Journal of Atmospheric and*  
769 *Oceanic Technology*, 19(2), 183–204. [https://doi.org/10.1175/1520-0426\(2002\)019<0183:EIMOBO>2.0.CO;2](https://doi.org/10.1175/1520-0426(2002)019<0183:EIMOBO>2.0.CO;2)
- 770 Eilander, D., Couasnon, A., Leijnse, T., Ikeuchi, H., Yamazaki, D., Muis, S., Dullaart, J., Haag, A., Winsemius, H. C., &  
771 Ward, P. J. (2023). A globally applicable framework for compound flood hazard modeling. *Natural Hazards and Earth*  
772 *System Sciences*, 23(2), 823–846. <https://doi.org/10.5194/nhess-23-823-2023>
- 773 Eilander, D., de Goede, R., Leijnse, T., van Ormondt, M., Nederhoff, K., & Winsemius, H. C. (2024). HydroMT-SFINCS  
774 (v1.1.0). Zenodo. <https://doi.org/10.5281/zenodo.13693006>
- 775 Jelesnianski, C. P. ., Chen, J., & Shaffer, W. A. . (1992). SLOSH : Sea, Lake, and Overland Surges from Hurricanes. NOAA

- 776 Technical Report, April.
- 777 Kennedy, A. B., Wirasact, D., Begmohammadi, A., Sherman, T., Bolster, D., & Dietrich, J. C. (2019). Subgrid theory for  
778 storm surge modeling. *Ocean Modelling*, 144, 101491. <https://doi.org/10.1016/j.ocemod.2019.101491>
- 779 Lazarus, E. D., & Constantine, J. A. (2013). Generic theory for channel sinuosity. *Proceedings of the National Academy of  
780 Sciences*, 110(21), 8447–8452. <https://doi.org/10.1073/pnas.1214074110>
- 781 Leijnse, T., van Ormondt, M., Nederhoff, K., & van Dongeren, A. (2021). Modeling compound flooding in coastal systems  
782 using a computationally efficient reduced-physics solver: Including fluvial, pluvial, tidal, wind- and wave-driven  
783 processes. *Coastal Engineering*, 163, 103796. <https://doi.org/https://doi.org/10.1016/j.coastaleng.2020.103796>
- 784 Lesser, G. R., Roelvink, D., van Kester, J. a. T. M., & Stelling, G. S. (2004). Development and validation of a three-dimensional  
785 morphological model. *Coastal Engineering*, 51(8–9), 883–915. <https://doi.org/10.1016/j.coastaleng.2004.07.014>
- 786 Luettich, R. A., Westerink, J. J., & Scheffner, N. W. (1992). ADCIRC: An Advanced Three-Dimensional Circulation Model  
787 for Shelves Coasts and Estuaries, Report 1: Theory and Methodology of ADCIRC-2DDI and ADCIRC-3DL, Dredging  
788 Research Program Technical Report DRP-92-6. In *Coastal Engineering Research Center (U.S.), Engineer Research and  
789 Development Center (U.S.). (Issue 32466, pp. 1–137)*. <https://erdc-library.erd.c.dren.mil/jspui/handle/11681/4618>
- 790 McGranahan, G., Balk, D., & Anderson, B. (2007). The rising tide: assessing the risks of climate change and human settlements  
791 in low elevation coastal zones. *Environment and Urbanization*, 19(1), 17–37.  
792 <https://doi.org/10.1177/0956247807076960>
- 793 Ramirez, J. A., Rajasekar, U., Patel, D. P., Coulthard, T. J., & Keiler, M. (2016). Flood modeling can make a difference:  
794 Disaster risk-reduction and resilience-building in urban areas. *Hydrology and Earth System Sciences Discussions*,  
795 November, 1–21. <https://doi.org/10.5194/hess-2016-544>
- 796 Rong, Y., Bates, P., & Neal, J. (2023). An improved subgrid channel model with upwind-form artificial diffusion for river  
797 hydrodynamics and floodplain inundation simulation. *Geoscientific Model Development*, 16(11), 3291–3311.  
798 <https://doi.org/10.5194/gmd-16-3291-2023>
- 799 Sebastian, A., Bader, D. J., Nederhoff, K., Leijnse, T., Bricker, J. D., & Aarninkhof, S. G. J. (2021). Hindcast of pluvial, fluvial  
800 and coastal flood damage in Houston, TX during Hurricane Harvey (2017) using SFINCS. *Natural Hazards*, 2017.  
801 <https://doi.org/10.1007/s11069-021-04922-3>
- 802 Sehili, A., Lang, G., & Lippert, C. (2014). High-resolution subgrid models: background, grid generation, and implementation.  
803 *Ocean Dynamics*, 64(4), 519–535. <https://doi.org/10.1007/s10236-014-0693-x>
- 804 Stelling, G. S., & Duinmeijer, S. P. A. (2003). A staggered conservative scheme for every Froude number in rapidly varied  
805 shallow water flows. *International Journal for Numerical Methods in Fluids*, 43(12), 1329–1354.  
806 <https://doi.org/10.1002/fld.537>
- 807 van Ormondt, M., Leijnse, T., Nederhoff, K., de Goede, R., van Dongeren, A., Bovenschen, T., & van Asselt, K. (2024).  
808 SFINCS: Super-Fast INundation of CoastS model (2.1.1 Dollerup Release 2024.01).  
809 Zenodo. <https://doi.org/10.5281/zenodo.13691619>
- 810 van Ormondt, M., Nederhoff, K., & Van Dongeren, A. (2020). Delft Dashboard: a quick setup tool for hydrodynamic models.

- 811 Journal of Hydroinformatics, 22(3), 510–527. <https://doi.org/10.2166/hydro.2020.092>
- 812 Volp, N. D., Van Prooijen, B. C., & Stelling, G. S. (2013). A finite volume approach for shallow water flow accounting for  
813 high-resolution bathymetry and roughness data. *Water Resources Research*, 49(7), 4126–4135.  
814 <https://doi.org/10.1002/wrcr.20324>
- 815 Vousdoukas, M. I., Voukouvalas, E., Annunziato, A., Giardino, A., & Feyen, L. (2016). Projections of extreme storm surge  
816 levels along Europe. *Climate Dynamics*, 47(9–10), 3171–3190. <https://doi.org/10.1007/s00382-016-3019-5>
- 817 Warren, I. R., & Bach, H. K. (1992). MIKE 21: a modelling system for estuaries, coastal waters and seas. *Environmental  
818 Software*, 7(4), 229–240. [https://doi.org/10.1016/0266-9838\(92\)90006-P](https://doi.org/10.1016/0266-9838(92)90006-P)
- 819 Woodruff, J. L., Dietrich, J. C., Wirasaet, D., Kennedy, A. B., Bolster, D., Silver, Z., Medlin, S. D., & Kolar, R. L. (2021).  
820 Subgrid corrections in finite-element modeling of storm-driven coastal flooding. *Ocean Modelling*, 167, 101887.  
821 <https://doi.org/10.1016/j.ocemod.2021.101887>
- 822 Woodruff, J., Dietrich, J. C., Wirasaet, D., Kennedy, A. B., & Bolster, D. (2023). Storm surge predictions from ocean to  
823 subgrid scales. *Natural Hazards*, 117(3), 2989–3019. <https://doi.org/10.1007/s11069-023-05975-2>
- 824 Yu, D., & Lane, S. N. (2011). Interactions between subgrid-scale resolution, feature representation and grid-scale resolution  
825 in flood inundation modelling. *Hydrological Processes*, 25(1), 36–53. <https://doi.org/10.1002/hyp.7813>
- 826 Yu, D., & Lane, S. N. (2006). Urban fluvial flood modelling using a two-dimensional diffusion-wave treatment, part 2:  
827 development of a subgrid-scale treatment. *Hydrological Processes*, 20(7), 1567–1583. <https://doi.org/10.1002/hyp.5936>
- 828